# *Simulation of Bubble Rising Flows by the Level Set Method*

**Ming-Jiu NI*, Satoru KOMORI****
**Department of Mechanical Engineering**
**Kyoto University, Kyoto, 606-8501, JAPAN**

***Abstract**:* The high accuracy variable density RKCN projection method is developed to do the computation of the unsteady interfacial flows with a large density variation, in which the 3-stage low-storage Runge-Kutta technique and 2nd-order semi-implicit Crank-Nicholson technique are employed to temporally update the convective and diffusion term respectively. The level set approach is employed to implicitly capture the interface for bubble rising flows. A re-initialization equation of level set function is solved to keep the level set function as a distance function from the front of interface. Especially a method with a variable time-step size has been presented to discretize the reinitialization equation to enforce the total mass conservation for the computation of incompressible interfacial flows by the level set approach.

Three-dimensional bubble rising flows in a liquid closed with a rectangle channel are studied numerically by the present method. The flow mechanisms for bubble rising flows with different density ratios; Weber and Reynolds numbers are discussed. It also validates the numerical analysis of Chen et al. [5] for the bubble rising flows closed with a cylinder.

## ***1. Introduction***

The numerical simulation of interfacial flows is of quite importance in investigating the transport phenomena appearing in environmental, geophysical and industrial flows. The interfacial flow involves the study not only on hydrodynamics in single phase, but also on the interface of the two or more immiscible and miscible fluids.

Instead of explicitly tracking the interface of the front-tracking method [17], the level set approach intends implicitly capture the interface by introducing a smooth level set function $\phi$, with the zero level set as the interface and positive as outside the interface and negative inside the interface. Considering the following equation:

$$\frac{\partial \phi}{\partial t} + u_i \frac{\partial \phi}{\partial x_i} = 0 \tag{1}$$

which will evolve the zero level of $\phi = 0$ exactly as the actual interface moves. The physical variants can be expressed as:

$$\rho = \begin{cases} \rho_1 & if \quad \phi > 0 \\ \rho_2 & if \quad \phi < 0 \\ 0.5(\rho_2 + \rho_1) & if \quad \phi = 0 \end{cases} \quad \mu = \begin{cases} \mu_1 & if \quad \phi > 0 \\ \mu_2 & if \quad \phi < 0 \\ 0.5(\mu_2 + \mu_1) & if \quad \phi = 0 \end{cases} \tag{2}$$

To keep the level set function as a distance function from the front, an approach based on solving the hyperbolic partial differential equation has been presented in [16]. The reinitialization equation is:

$$\phi_t = sign_\varepsilon(\phi_0)(1 - |\nabla \phi|) \tag{3}$$

$$\phi(\vec{x}, 0) = \phi_0(\vec{x}) \tag{4}$$

where $|\nabla \phi| = \sqrt{\phi_x^2 + \phi_y^2 + \phi_z^2}$, and the sign function $sign_\varepsilon(\phi_0) = 2(H_\varepsilon(\phi_0) - 1/2)$ with the Heaviside function $H_\varepsilon(\phi)$ included in.

Unlike $\rho$, and $\mu$ which change sharply at the front, the level set function is a smooth function. The equation (1) is more easily solved numerically by employing the high-resolution discretization schemes for the convective term. The simplicity of the numerical solution for the Eq.(1), especially for the computation of the curvature $k$ is the advantage of the level set approach over the VOF method [6].

---

* JSPS Research Fellow, E-mail: mjni9999@ip.media.kyoto-u.ac.jp
** Professor, Kyoto University, E-mail: komori@mech.kyoto-u.ac.jp

We know the total mass is conservation in time for incompressible flows. However, the numerical discretization of the level set formulation does not preserve the property in general. Hou et al. [7] has found that a considerable amount of total mass is lost in time even by the above re-initialization of the level set function. To ensure the mass conservative, Sussman & Fatemi [15] presented the modified re-initialization equation.

On the numerical methods for unsteady variable density incompressible Navier-Stokes equations, the variable density BCG method [2] is often employed to do the simulation of interfacial flows. However, due to the employment of the Godunov technique to update the convective term, it is some difficult to spatially discretize the convective term with high accuracy schemes for this method. Kothe and Mjolsness [8] conducted the computation of interfacial flows by the MAC method, in which the explicit updating of the convective and diffusion terms is not stable with a big time-step size. Chen et al. [5] employed the SIMPLE method for the numerical simulation of bubble rising flows. Sato et al. [11] employed the first-order fully explicit MAC method to do the direct simulation of droplet flows incorporating with MDF method to capture the interface. Son and Dhir [12] employed the projection method to do the numerical simulation of the boiling heat transfer incorporating with the level set approach for capturing the interface. However Both the methods of Sato et al. and Son et al. have only 1st-order temporal accuracy. For unsteady incompressible single-phase flows, the RKCN projection method is developed [9], in which the three-stage low-storage Runge-Kutta and 2nd-order semi-implicit Crank-Nicholson techniques are employed to update the convective and diffusion terms respectively. Here the RKCN projection method for single-phase unsteady incompressible flows will be further extended to solve variable density immiscible interfacial flows.

By employing the level set method to simulate bubble rising flows in a liquid in this paper, the physical model and numerical algorithms are presented in section 2. The bubble rising flows with different density ratios, Reynolds numbers and Weber numbers are numerically studied in section 3. The conclusions are presented in section 4.

## *2. Physical Models and Numerical Algorithms*

### 2.1 Governing Equations

For numerical simulation of interfacial flows using the VOF method, Brackbill et al. [3] presented a CSF (continuum surface force) model for surface tension force, in which the surface tension is reformulated as a volume force $\vec{F}_{sv}$. With the volume force $\vec{F}_{sv}$, surface tension effects at free surfaces are modeled as a body force in the momentum transport equations. For the level set approach, Chang et al. [4] derived a new formulation of the CSF model for surface tension based on the smooth level set function as $\vec{F}_{SV} = k(\phi)\delta_\alpha(\phi)\nabla\phi$ with the surface tension delta function $\delta_\varepsilon(\phi) = \partial H_\varepsilon(\phi)/\partial\phi$ and the front curvature $k(\phi) = \nabla\cdot(\nabla\phi/|\nabla\phi|)$. The Heaviside function $H_\varepsilon(\phi)$ is formulated as:

$$H_\varepsilon(\phi) = \begin{cases} 0 & if\ \phi < -\varepsilon \\ \frac{1}{2}\left[1 + \frac{\phi}{\varepsilon} - \frac{1}{\pi} sin\left(\frac{\pi\phi}{\varepsilon}\right)\right] & if\ |\phi| \le \varepsilon \\ 1 & if\ \phi > \varepsilon \end{cases}$$

By employing the CSF model of the surface tension force for the level set approach, the governing equations for an incompressible interfacial flow can be written as:

$$\frac{\partial u_i}{\partial x_i} = 0 \tag{5}$$

$$\frac{\partial u_i}{\partial t} = -\frac{1}{\bar{\rho}}\frac{\partial p}{\partial x_i} + \frac{\bar{\mu}}{\bar{\rho}\, Re}\frac{\partial^2 u_i}{\partial x_j \partial x_j} + S_i \tag{6}$$

$$\frac{\partial \phi}{\partial t} + u_i \frac{\partial \phi}{\partial x_i} = 0 \tag{7}$$

$$S_i = -\frac{\partial}{\partial x_j}(u_i u_j) - \frac{\vec{k}}{Fr} - \frac{k(\phi)\delta(\phi)\nabla\phi}{\bar{\rho} We} + \frac{1}{\bar{\rho}\, Re}\left(\frac{\partial u_i}{\partial x_j} + \frac{\partial u_j}{\partial x_i}\right)\frac{\partial \bar{\mu}}{\partial x_j} \tag{8}$$

with dimensionless groups of Reynolds, Froud & Weber numbers as $Re = \rho_1 LU/\mu_1$, $Fr = U^2/gL$, and

$We = \rho_1 L U^2 / \sigma$ respectively. $\bar{\mu} = \mu/\mu_1$, $\bar{\rho} = \rho/\rho_1$ are the dimensionless ratios of the viscosity and density. For simplicity, hereafter we will instead $\bar{\mu}$ and $\bar{\rho}$ with $\mu$ and $\rho$ respectively. To prevent the instability, it is necessary to smooth the values of the density $\rho$ and viscosity $\mu$ as:

$$\rho_\varepsilon(\phi) = \lambda_\rho + (1-\lambda_\rho) H_\varepsilon(\phi) \tag{9}$$

$$\mu_\varepsilon(\phi) = \lambda_\mu + (1-\lambda_\mu) H_\varepsilon(\phi) \tag{10}$$

where $\lambda_\rho = \rho_2/\rho_1$, $\lambda_\mu = \mu_2/\mu_1$, $H_\varepsilon(\phi)$ is the Heaviside function introduced above.

**2.2 Time Integration**

The RKCN high accuracy projection method developed in [9] for single-phase incompressible flow has second-order temporal accuracy. Here we extend the method to the variable density unsteady incompressible Navier-Stokes equations incorporating with the level set equation for the interfacial flows. The variable density RKCN projection method can be depicted as:

$$A_i^m \hat{u}_i^m = r_i^m - \left( \frac{\alpha^m}{\rho^{m-1}} \frac{\partial p^{m-1}}{\partial x_i} + \frac{\beta^m}{\rho^{m-2}} \frac{\partial p^{m-2}}{\partial x_i} \right) \tag{11}$$

$$\tilde{u}_i^m = \hat{u}_i^m + \Delta t \left( \frac{\alpha^m}{\rho^{m-1}} \frac{\partial p^{m-1}}{\partial x_i} + \frac{\beta^m}{\rho^{m-2}} \frac{\partial p^{m-2}}{\partial x_i} \right) \tag{12}$$

$$u_i^m = \tilde{u}_i^m - \Delta t \left( \frac{\alpha^m}{\rho^m} \frac{\partial p^m}{\partial x_i} + \frac{\beta^m}{\rho^{m-1}} \frac{\partial p^{m-1}}{\partial x_i} \right) \tag{13}$$

$$\alpha^m \frac{\partial}{\partial x_i} \left[ \frac{1}{\rho^m} \frac{\partial p^m}{\partial x_i} \right] = \frac{1}{\Delta t} \frac{\partial \tilde{u}_i^m}{\partial x_i} - \beta^m \frac{\partial}{\partial x_i} \left[ \frac{1}{\rho^{m-1}} \frac{\partial p^{m-1}}{\partial x_i} \right] \tag{14}$$

$$\phi^{m+1} = \phi^m - \Delta t \left( \alpha^{m+1} u_i^m \frac{\partial \phi^m}{\partial x_i} + \beta^{m+1} u_i^{m-1} \frac{\partial \phi^{m-1}}{\partial x_i} \right) \tag{15}$$

where

$$A_i^m = \frac{1}{\Delta t} \left[ 1 - \frac{\gamma^m \Delta t}{Re} \frac{\mu^m}{\rho^m} \frac{\partial^2}{\partial x_j \partial x_j} \right] \tag{16}$$

$$r_i^m = \frac{1}{\Delta t} \left[ 1 - \frac{\gamma^m \Delta t}{Re} \frac{\mu^{m-1}}{\rho^{m-1}} \frac{\partial^2}{\partial x_j \partial x_j} \right] u_i^{m-1} - \alpha^m [S_i]^{m-1} - \beta^m [S_i]^{m-2} \tag{17}$$

$\alpha^m = \langle \frac{8}{15}, \frac{5}{12}, \frac{3}{4} \rangle$, $\beta^m = \langle 0, -\frac{17}{60}, -\frac{5}{12} \rangle$ and $\gamma^m = \langle \frac{4}{15}, \frac{1}{15}, \frac{1}{6} \rangle$. The velocity components and pressure in the intermediate velocities equation at the first sub-step are $u_i^{-1} = 0$, $p^{-1} = 0$ $(m-2=-1)$ and $u_i^0 = u_i^n$, $p^0 = p^n$ $(m-1=0)$. At the third step, $u_i^3 = u_i^{n+1}$ and $p^3 = p^{n+1}$, which are the updated velocities and pressure for the next time level $n+1$.

**2.3 Reinitialization for Level Set Function**

In general, even if the level set function $\phi$ is initialized as a signed distance from the interface front, it will not remain a distance function at later time. For large time computations, keeping the level set function as a distance function will be advantage in the computational of surface tension, which is difficult to compute near a steep gradient in the distance function. In the meantime, the distance function of $\phi$ will ensure that the front has a finite thickness for all time, and the values for $\rho(\phi)$ will not be greatly distorted with $\nabla\phi$ equal to one. Sussman et al. [16] presented the reinitialization equation as Eqs.(3) and (4), which can be reformulated as:

$$\phi_t + \boldsymbol{w} \cdot \nabla\phi = sign_\varepsilon(\phi_0) \tag{18}$$

where

$$\boldsymbol{w} = sign_\varepsilon(\phi_0) \frac{\nabla\phi}{|\nabla\phi|} \tag{19}$$

For level set approaches, another important issue is mass conservation. We know the total mass is conservation in time for an incompressible flow. Theoretically, the solution $\phi$ of Eqs.(18) and (19) will have the same sign and the same zero level set as $\phi_0$, which means the interface will not move as time marching for the solution of Eqs.(18) and (19). Away from the interface $\phi$ will converge to $|\nabla\phi| = 1$.

Therefore it will converge to the actual distance. The unmoved interface with $|\nabla\phi| = 1$ will ensure the total mass conservation. However, the numerical discretization of the reinitialization equation of the level set function will not preserve the property in general. Chang et al. [4] concluded the above re-initialization procedure for the level set function can just ensure that the $\phi$ to be a distance function from the front. Hou et al. [7] has also found that a considerable amount of total mass is lost in time by the above re-initialization of the level set function.

In fact, the half-discretized form of Eq.(18) can be written as

$$\phi^{n+1} = \phi^n + \Delta t_0 sign_\varepsilon(\phi_0)\left(1 - |\nabla\phi^n|\right) \tag{20}$$

For the case of $|\nabla\phi| > 1$ nearby the interface, we can find from Eq.(20) that a big time step cannot ensure the discretized value of the level set function has a same sign as the initial value. That means the large time step cannot keep the conservation of the volume nearby the interface for the case of $|\nabla\phi| > 1$. To overcome this difficulty, the variable time-step size method can be presented to conduct the solution of Eqs.(18) and (19), the criterion for choosing the time step is to preserve the total volume of interface.

The variable time step can be formulated as:

$$\Delta t = \Delta t_0 - \Delta t_0' / a \qquad a = |\nabla\phi^n| - 1 \tag{21}$$

$$\Delta t_0' = \frac{\int_{\Omega_{ijk}} \delta(\phi) sgn(\phi_0) a}{\int_{\Omega_{ijk}} [\delta(\phi)]^2 \, sgn(\phi_0)(1+a)(1+a^2)(1+a^4)} \tag{22}$$

To accelerate the convergence, a two-stage Runge-Kutta technique with a larger time-step size can be taken in solving the re-initialization equation. The re-initialization procedure can be stopped when the relative error between the total mass at the current time and the initial mass is less than $10^{-6}$. According to our computation, the average mass error using the variable time-step size technique (20-22) was greatly less than that using original re-initialization technique Eq.(20) with the constant time-step size.

In summary, it is possible to keep the level set function as a distance function and to enforce the mass conservation in time by using various re-initialization techniques. The numerical diffusion introduces in the advection step for the smooth level set function does not diffuse the front. This would not have been the case if we used a high-resolution capturing scheme to solve the density equation directly, since the density has a contact discontinuity across the interface.

## ***3. Simulation of Bubble Rising Flows***

The rise and deformation of bubbles in a liquid with the initial bubble radius $R_0$ are simulated by the above-developed methods. The non-dimensional governing equation is formulated as in Eqs.(3)~(6) with dimensionless groups of Reynolds, Froud and Weber numbers as $Re = \rho_1 g^{\frac{1}{2}} R_0^{\frac{3}{2}} / \mu_1$, $Fr = 1$, and $We = \rho_1 g R_0^2 / \sigma$. The bubble rises driven by the buoyancy force. From previous numerical and experimental results, we know that the Weber number, Reynolds number and the ratio of density will have big effects on the rising and deformation of the bubble.

In a 3-D rectangle channel with free-surface boundary on the top and walls on the other sides, an initially stationary spherical bubble is considered with the initial condition $u_i(t=0) = 0$ and boundary conditions $u_3 = 0$, $\partial u_i / \partial x = 0$ $(i = 1,2)$ on the top surface and $u_i = 0$ on the solid walls. The computation is finished using the variable density RKCN projection method incorporating with the level set method. Collocated grid system [18] with the meshes of $65 \times 65 \times 85$ is utilized to do the numerical simulation of bubble rising flows in a liquid by the supercomputer in Kyoto University.

The numerical results in a 3-D rectangular channel are similar as the results in a cylinder channel [5]. For a large density ratio flow, figure 1 illustrates that the bubble begins to rise owing to buoyancy. The pressure difference between the top and low surface drives the bubble rise and forms the vortex sheet at the surface, which induces the jet motion to push the water into the bubble from below at $\tau = 0.5$. Due to the effect of the jet, the velocity difference between the top surface and the lower surface is formed. The velocity difference results in the formation of the bubble cap at $\tau = 0.75$. Further, it results in the lower surface approaching the top surface of the bubble cap at $\tau = 1.5$. As the time marching, the jet motion results in the lower surface piercing the top surface of the bubble eventually, which can be seen in figure 5.

An increase in the density ratio leads to an increase of the net force of the difference between the buoyancy force and gravity, which will result in a higher rise velocity for the bubble. To investigate the effect of the density ratio on the bubble rising, the numerical results for three density ratios of 1000, 80 and 5 were presented in figures 3, 5 and 6, in which the Reynolds number, Weber number and viscosity ratio are kept constant. For the higher density ratios of $\rho_l/\rho_g = 1000$ and 80, the development of bubble shape with time is similar. As time marching, the piecing of the lower surface into the top surface at $\tau = 2.0$ results in the formation of the toroid in figures 3 and 6. For the lower density ratio of $\rho_l/\rho_g = 5$, figure 5 also illustrates the formation of the toroid, however it has been delayed to $\tau = 3.0$. In the computation of Chen et al.[5] for the case of lower density ratio, the toroid is not formed until the $\tau = 4.0$. We also find from the vertical velocity distributions in figures 3, 5 and 6 that a higher density ratio results in a faster rise of the bubble when the bubble has not undergone a significant shape change.

From equations (4) and (6), the effect of surface tension on the bubble dynamics can be investigated by changing the values of the Weber number. Here the role of surface tension in the formation of a toroidal bubble has been studied with Weber numbers as 5, and 50 while the Reynolds number and the ratios of density and viscosity are kept as constants (Re=100, $\rho_l/\rho_g = 80$, $\mu_l/\mu_g = 80$). Figures 3, and 4 illustrate the effect of surface tension on the development of the bubble. At the lowest Weber number (We=5) in figure 4, owing to the high surface tension, the water jet formed below the bubble is unable to penetrating the upper surface and an elliptical bubble forms. As the decrease of the surface tension for the cases of We=50 in figures 3, the toroidal bubbles form at $\tau = 2.0$. Nearby the upper boundary the rising velocity will be reduced due to the restriction of the boundary condition of $u_3 = 0.0$, which can be regarded as the wall repulsion effect. The vertical velocity profiles at the mid-surface for the horizontal-vertical surface are also shown in the figures 3, and 4. The primary effect of a reduction in surface tension on the bubble dynamics is manifested as a change in shape of the bubble from elliptical to toroidal.

The effect of the viscous force on the motion of the bubble can also been investigated by varying the Reynolds number in Eqs.(4) and (6), while the other flow parameters are kept as constants with We=50, , $\rho_l/\rho_g = 80$, $\mu_l/\mu_g = 80$. For the low Reynolds number flow of Re=10, due to the big effect of the viscous force, the liquid jet below the bubble is very weak and the bubble rises as a cap in figures 2. As increase of Reynolds number to Re=100, the effect of the buoyancy is much greater than the effect of the viscous force. The jet motion below the bubble surface drives the lower surface to pierce the upper surface and form the toroid in at $\tau = 2.0$ figure 3. The results are in consistent with the classical analytical results in [1], in which the low Reynolds number has been shown to be able to preserve the spherical formation for the drop falling flow in a liquid. The vertical velocity distributions with different Reynolds numbers are also shown in figures 2 and 3. In the region below the bubble, the velocity contours vary significantly as the Reynolds number is varied. A higher Reynolds number results in a stronger jet in the region below the bubble.

## ***4. Summaries and Conclusions***

The high-order variable density RKCN projection method has been developed to simulate the unsteady variable density incompressible Navier-Stokes equations, in which the 3-stage low-storage Runge-Kutta and 2$^{nd}$-order semi-implicit Crank-Nicholson techniques are employed to update the convective and diffusion terms for simplicity and stability respectively. The four-level multigrid technique has been employed to enforce the divergence-free velocity for incompressible flows. The hyperbolic equation for the level-set function has been incorporated to capture the interface automatically with high accuracy. A re-initialization technique based on the solving of PDE has been used to keep the level set function as a distance function from the interface front, and a variable time-step size method has been developed to enforce the total mass conservation for the level set method of incompressible interfacial flows. The TVD and ENO schemes have been employed to spatially discretize the convective terms of the evolving equation and the re-initialization equation of the level set function. The bubble rising flows in a 3-D rectangular channel with a large variation of density, different Weber and Reynolds numbers have been simulated using the above-developed methods. The bubble rising and deformation mechanisms have been presented, which is similar as the computation of bubble rising flows in a liquid closed with the cylinder channel by the VOF method in [5].

## ***Acknowledgments***

The first author acknowledges the financial support from the JSPS (Japan Society for the Promotion of Science).

## ***References***


1. Batchelor, G.K., 1967, *An Introduction to Fluid Dynamics*, Cambridge, Cambridge University Press
2. Bell, J.B., Marcus, D.L., 1992, J. Comput. Phys., Vol.101, pp: 334
3. Brackbill, J.U., Kothe, D.B., Zemach, C., 1992, J. Comput. Phys., Vol.100, No.2, pp: 335-54
4. Chang, Y.C., Hou, T.Y., Merriman, B., Osher, S., 1996, J. Comput. Phys., Vol.124, pp: 449-464
5. Chen, L., Garimella, S.V., Reizes, J.A., Leonardi, E., 1999, J. Fluid Mech., Vol.387, pp:61-96
6. Hirt, C.W., Nichols B.D., 1981, J. Comput Phys, Vol.39, No.1, pp:201-225
7. Hou, T.Y., Rosakis, P., LeFloch, P., 1999, J. Comput. Phys., Vol.150, pp:302-331
8. Kothe, D.B., Mjolsness, R.C., 1992, AIAA J, Vol.30, No.11, pp:2694-2700
9. Ni, M.-J., Komori, S., 2001, AIAA Paper 2001-0284
10. Osher, S., Sethin, J.A., 1988, J. Comput. Phys., Vol.79, No.1, pp:12
11. Sato, T., Jung, R.-T., Abe, S., 2000, ASME J Fluids Eng, Vol.122, No.3, pp:510-516
12. Sethian, J.A., 1996, Level Set Methods: Evolving Interfaces in Geometry, Fluid Mechanics, Computer Vision, and Materials Science, Cambridge University Press.
13. Son, G., Dhir, V.K., 1997, ASME J Heat Transfer, Vol.119, pp:525-533
14. Shu, C.-W., Osher, S., 1989, J. Comput. Phys., Vol.83, pp:32-78
15. Sussman, M., Fatemi, E., 1999, SIAM J Sci Comput, Vol.20, pp:1165-91
16. Sussman, M., Smereka, P., Osher, S., 1994, J. Comput. Phys., Vol.114, pp: 146-59
17. Unverdi, S.O., Tryggvason, G., 1992, J. Comput. Phys., Vol.100, pp:25-37
18. Zang, Y., Street, R.T., Koseff, J.R., 1994, J. Comput. Phys., Vol.114, pp:18-33


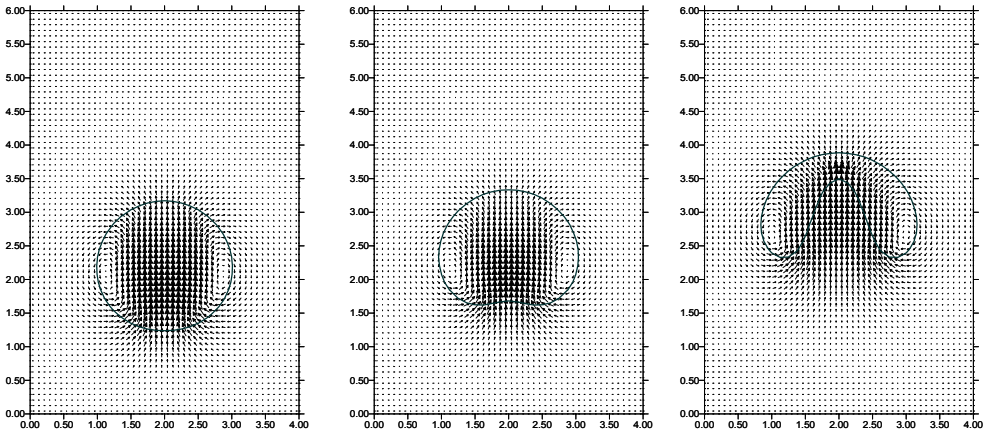


$\tau = 0.5$ $\tau = 0.75$ $\tau = 1.5$

Figure 1 Bubble Evolution Shapes and Velocity Vector Contours

for the Case of Re=100, We=50, $\rho_l / \rho_g = 1000$, $\mu_l / \mu_g = 80$

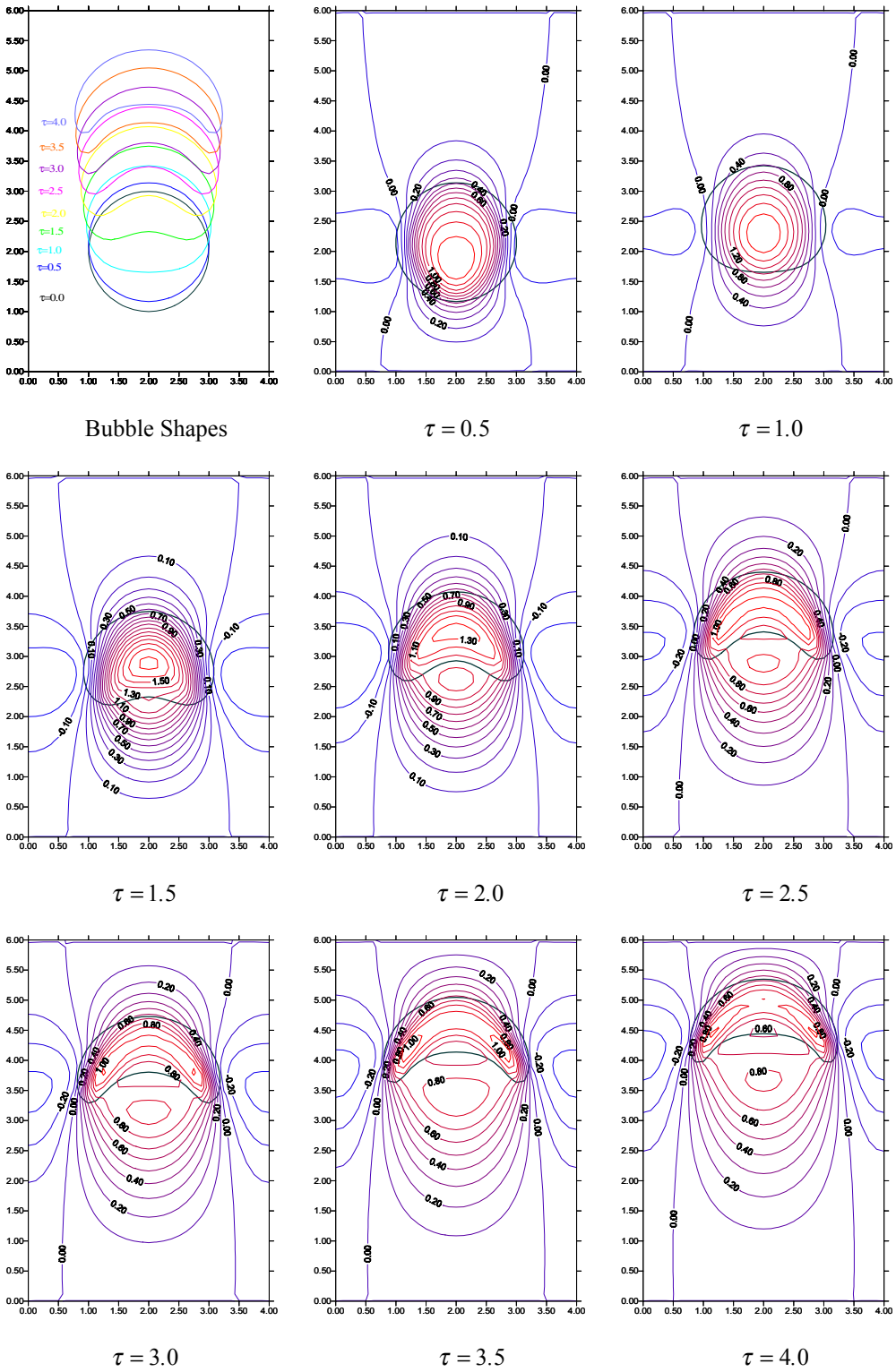


Figure 2 Bubble Evolution Shapes and Vertical Velocity Contours

for the case of Re=10, We=50, $\rho_l/\rho_g = 80$, $\mu_l/\mu_g = 80$

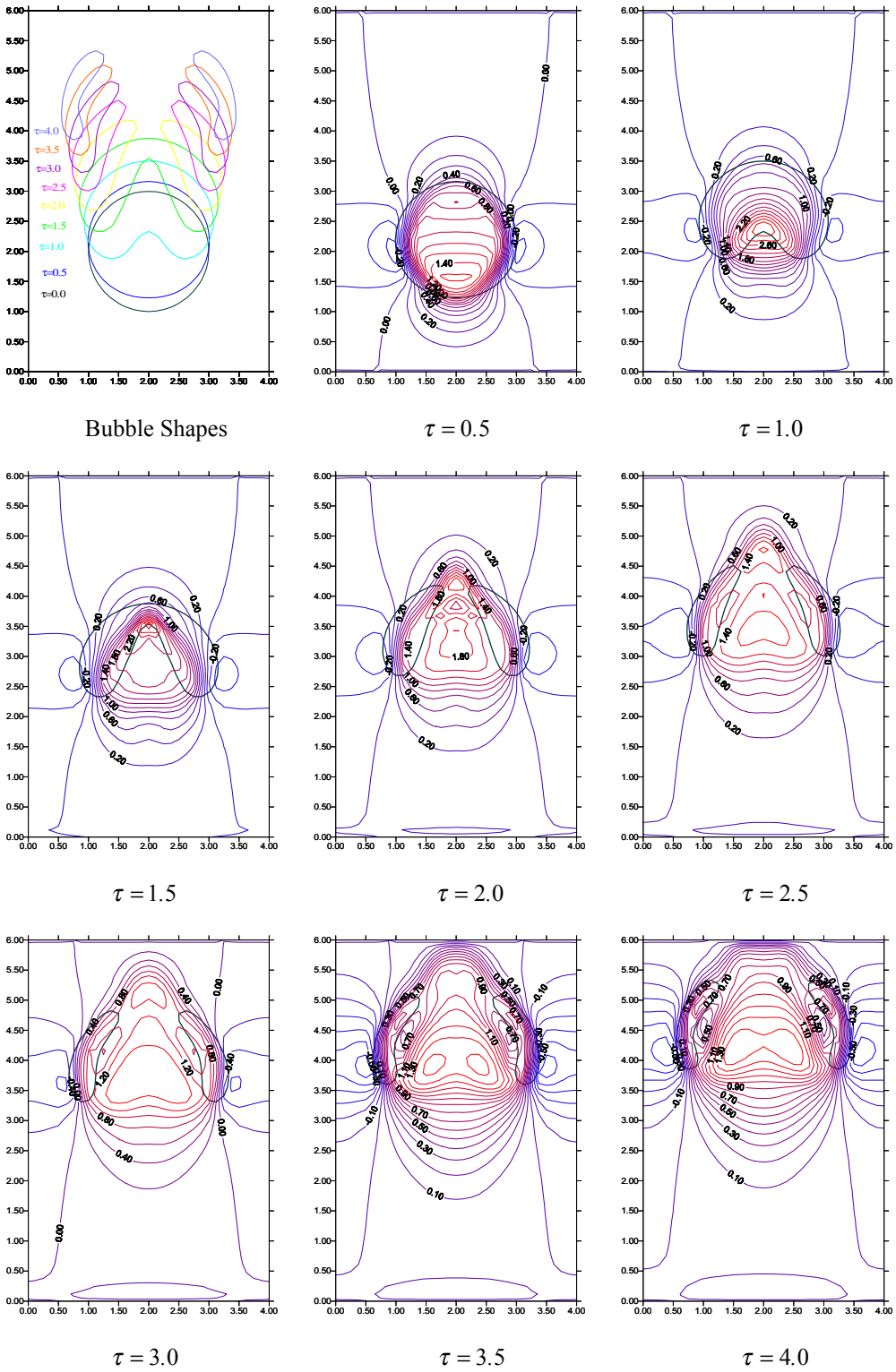


Figure 3 Bubble Evolution Shapes and Vertical Velocity Contours

for the case of Re=100, We=50, $\rho_l/\rho_g = 80$, $\mu_l/\mu_g = 80$

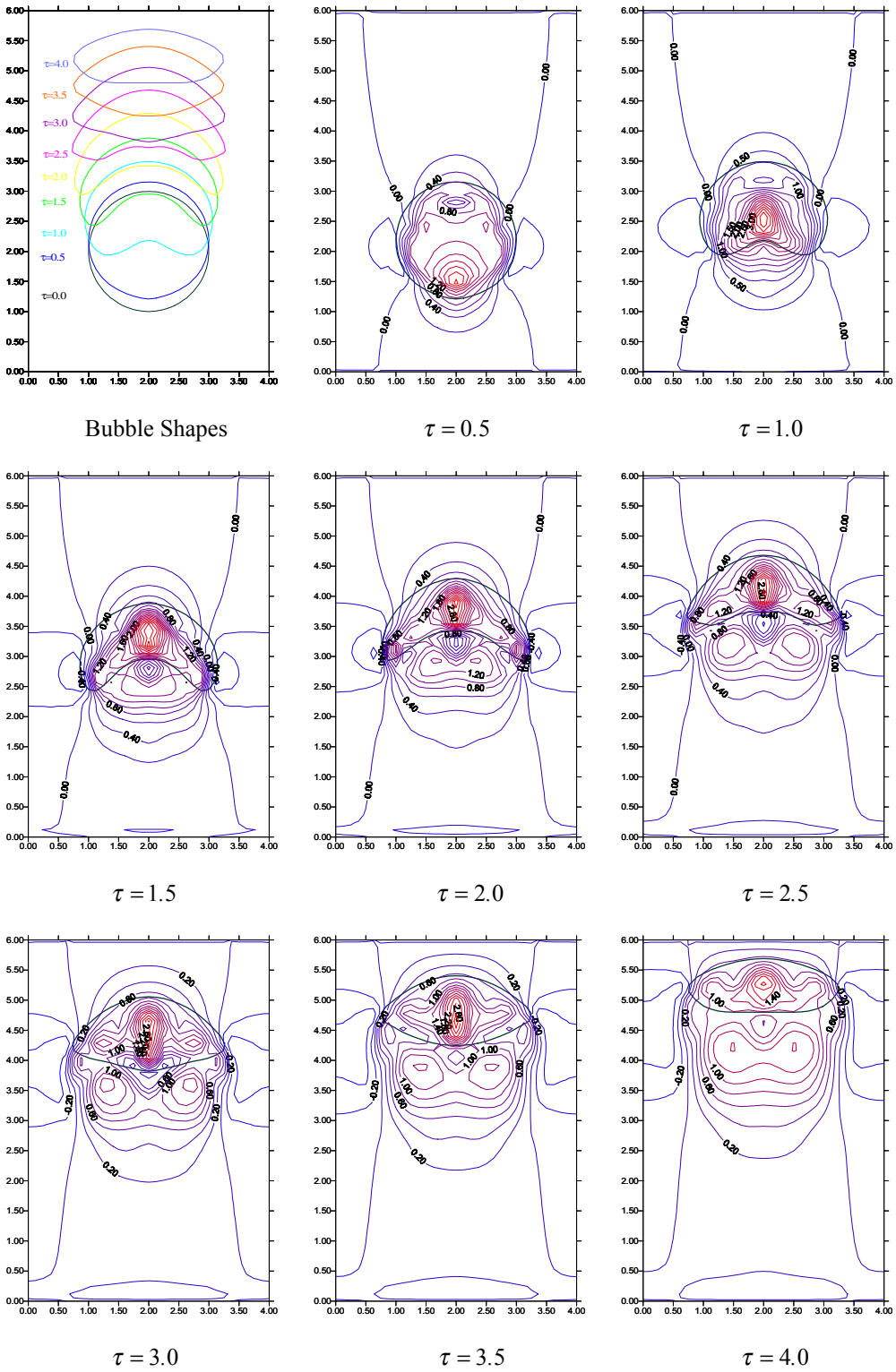


Figure 4 Bubble Evolution Shapes and Vertical Velocity Contours

for the case of Re=100, We=5, $\rho_l/\rho_g = 80$, $\mu_l/\mu_g = 80$

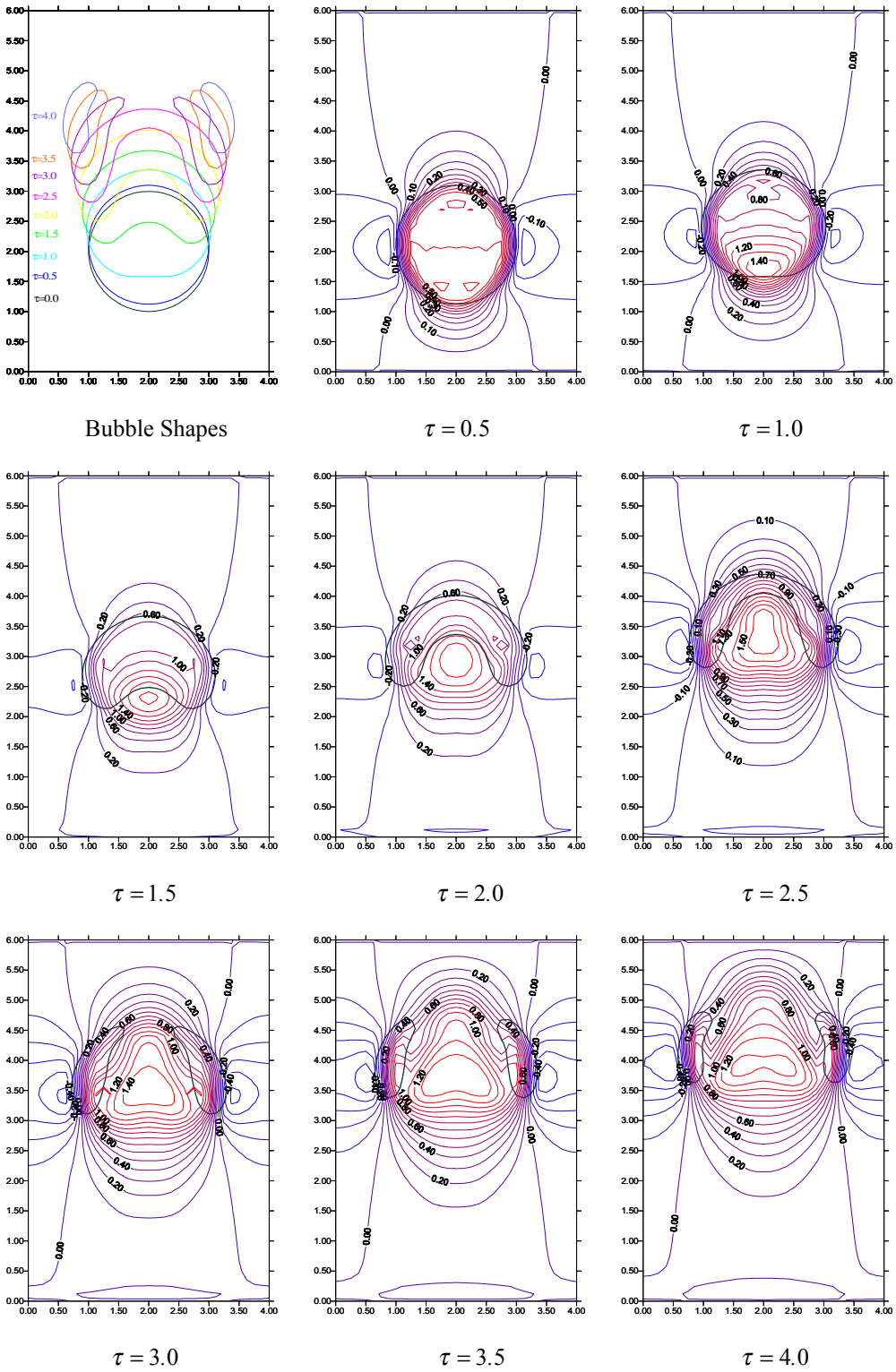


Figure 5 Bubble Evolution Shapes and Vertical Velocity Contours

for the case of Re=100, We=50, $\rho_l/\rho_g = 5$, $\mu_l/\mu_g = 80$

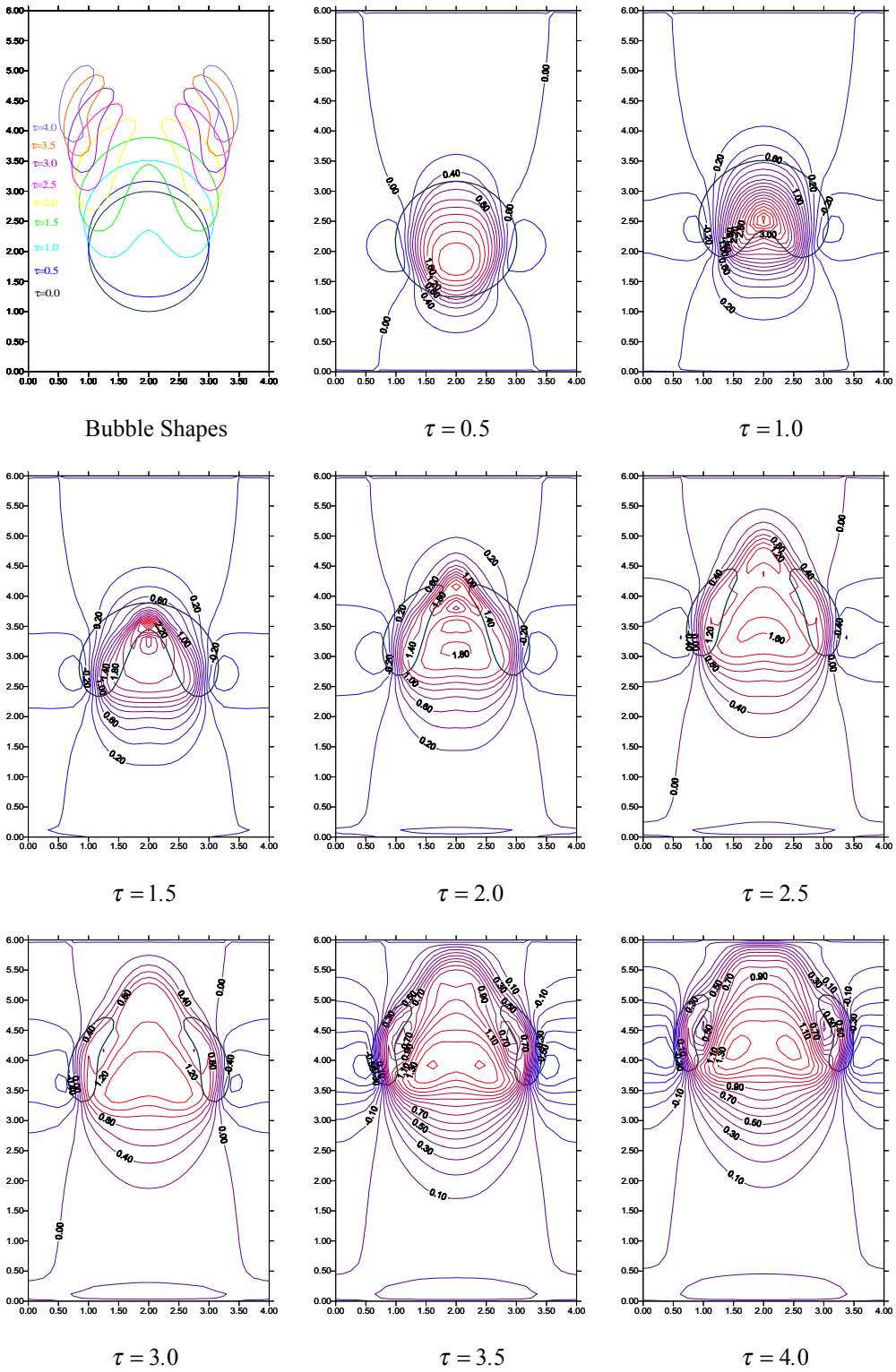


Figure 6 Bubble Evolution Shapes and Vertical Velocity Contours

for the case of Re=100, We=50, $\rho_l/\rho_g = 1000$, $\mu_l/\mu_g = 80$